Supplementary Materials

Mechanochemical process enhancing pore reconstruction for dense energy storage of carbon-based supercapacitors

Dongyang Wu[1], Fei Sun[1,*], Hua Wang[1], Yang Li[2], Boran Zhang[1], Chenglong Yang[2], Zhefan Wang[2], Jihui Gao[1], Guangbo Zhao[1]

[1]School of Energy Science and Engineering, Harbin Institute of Technology, Harbin 150001, Heilongjiang, China.

[2]Xí'an Thermal Power Research Institute Co., Ltd, Xí'an 710054, Shaanxi, China.

***Correspondence to:** Dr. Fei Sun, School of Energy Science and Engineering, Harbin Institute of Technology, No. 92 Xidazhi Street, Nangang District, Harbin 150001, Heilongjiang, China. E-mail: sunf@hit.edu.cn

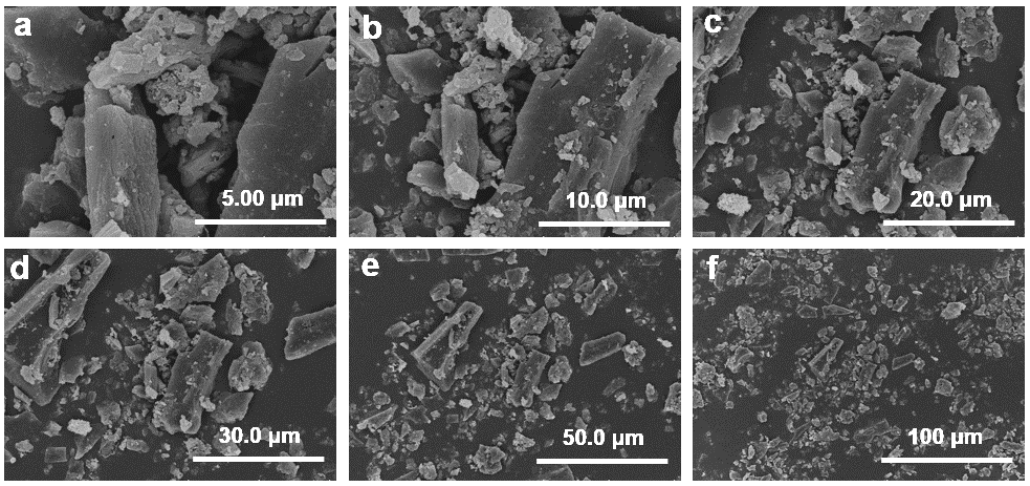

Figure S1 SEM images of CAC at different magnifications.

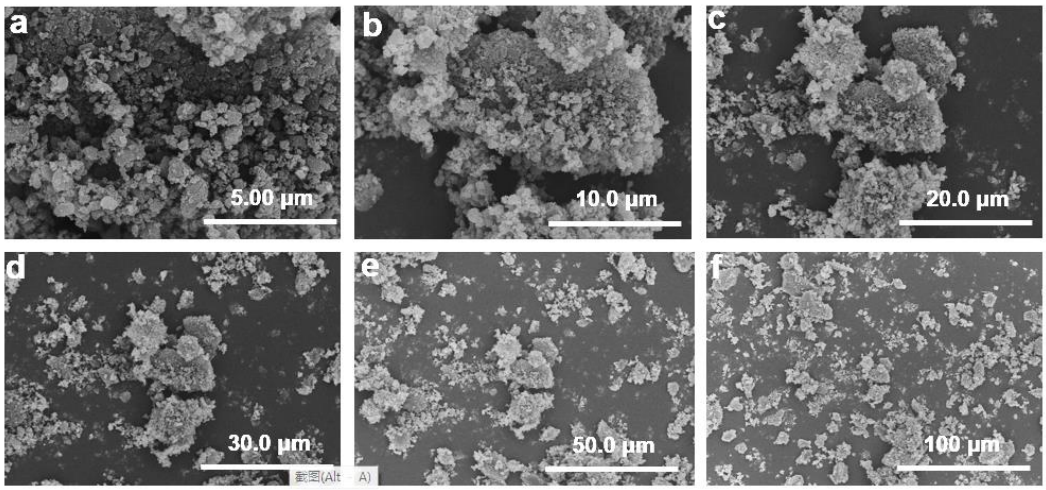

Figure S2 SEM images of CAC-1 at different magnifications.

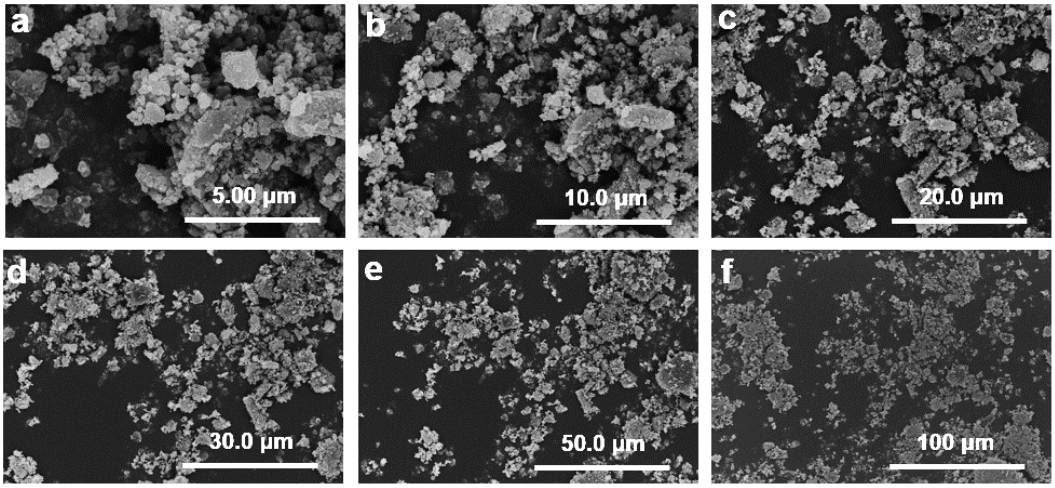

Figure S3 SEM images of CAC-4 at different magnifications.

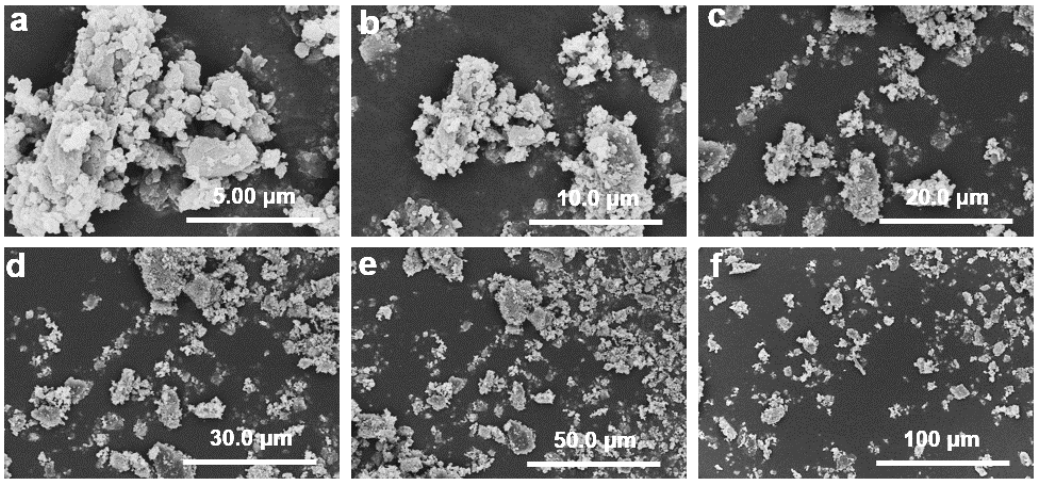

Figure S4 SEM images of CAC-8 at different magnifications.

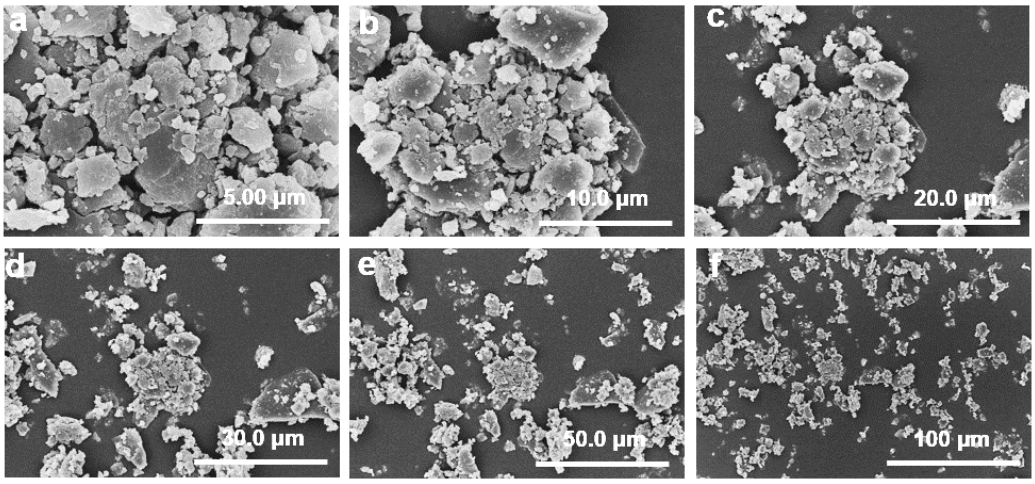

Figure S5 SEM images of CAC-12 at different magnifications.

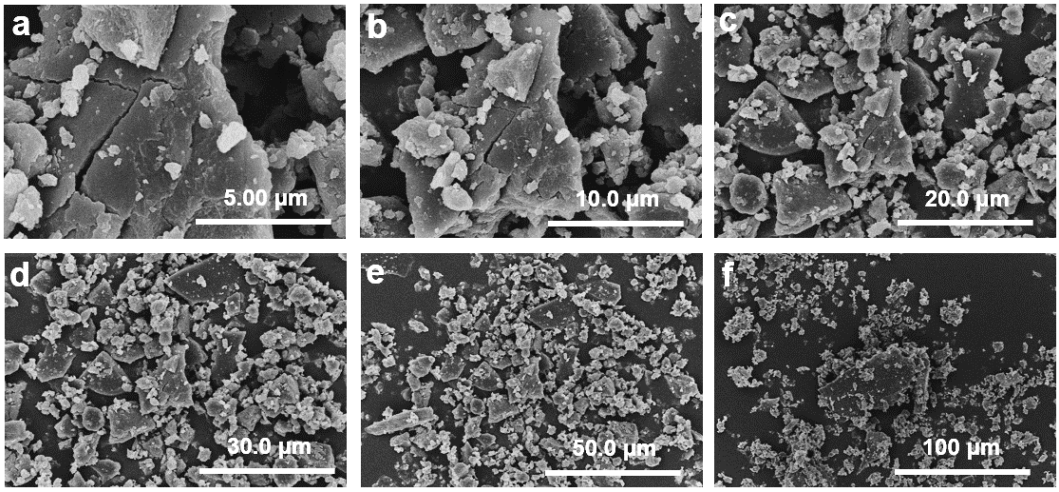

Figure S6 SEM images of CAC-24 at different magnifications.

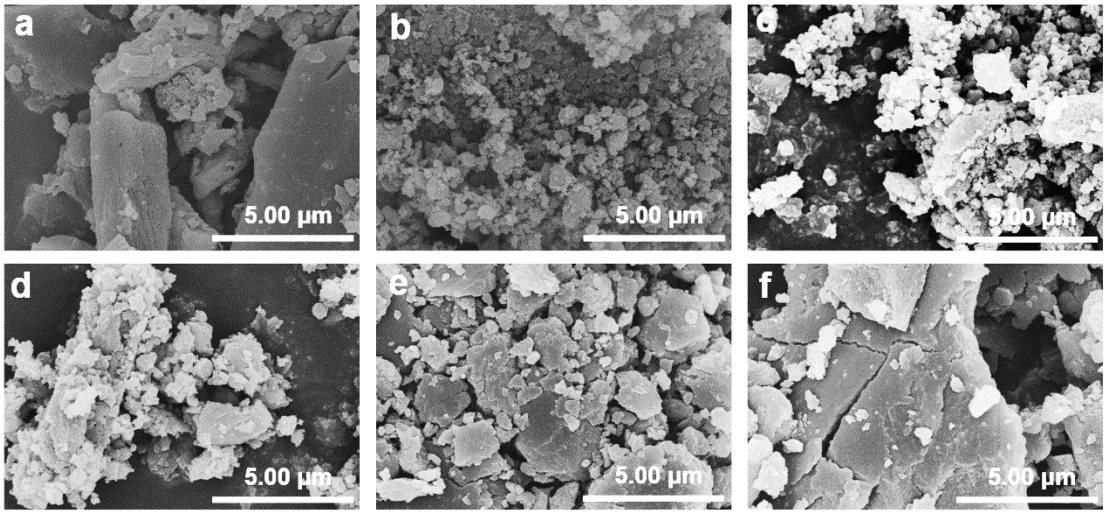

Figure S7 SEM images of CAC-*x* at same magnification.

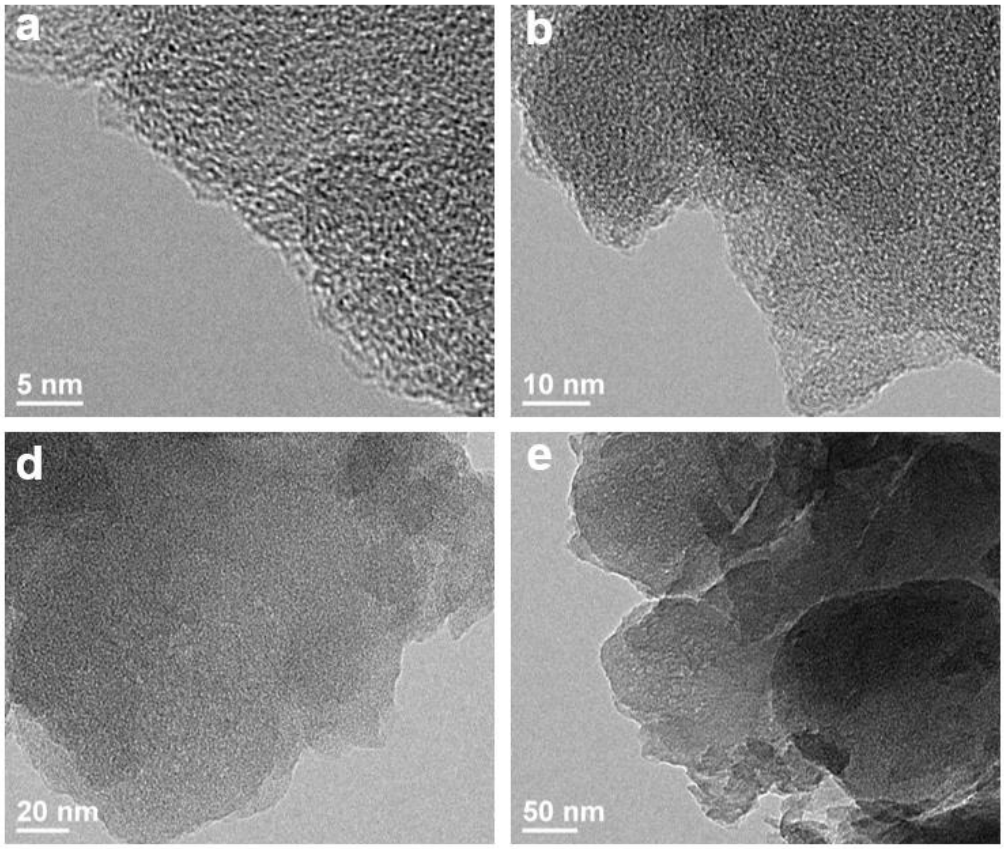

Figure S8 HRTEM images of CAC-24 at different magnifications.

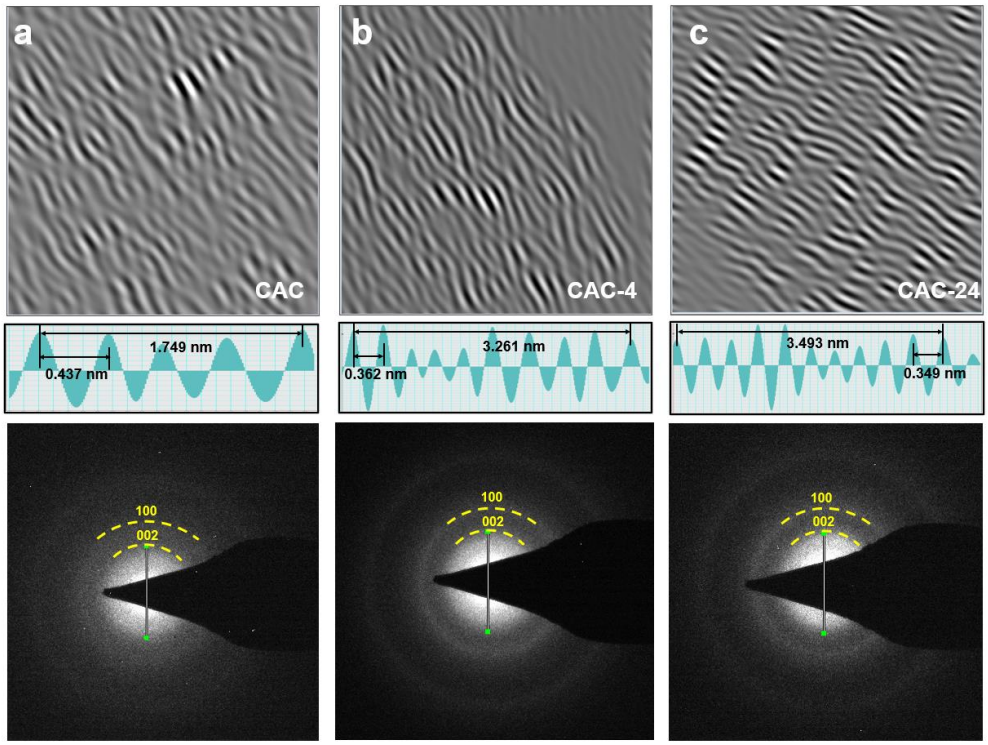

Figure S9 Lattice fringes and SAED of **a** CAC-0, **b** CAC-4 and **c** CAC-24.

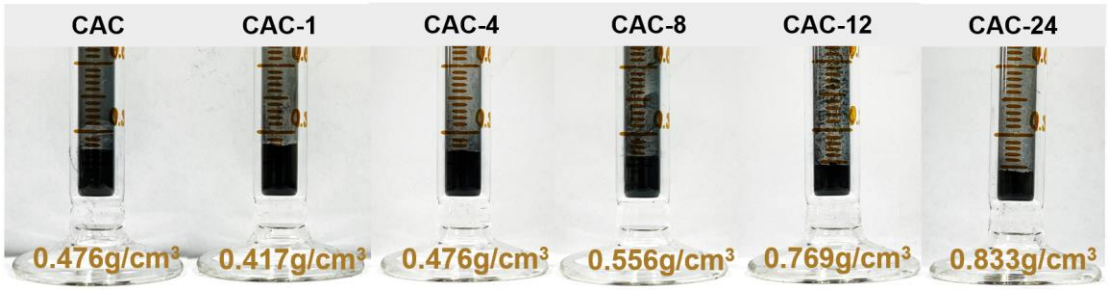

Figure S10 Vibration densities of CAC and CAC-*x*.

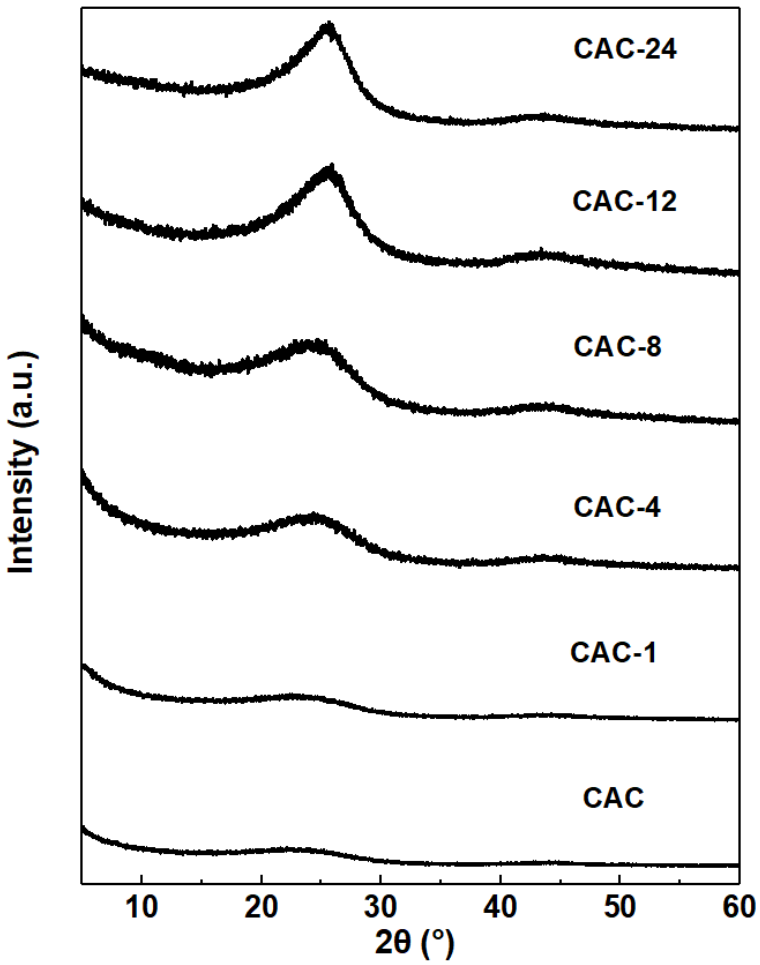

Figure S11 XRD patterns of CAC and CAC-*x*.

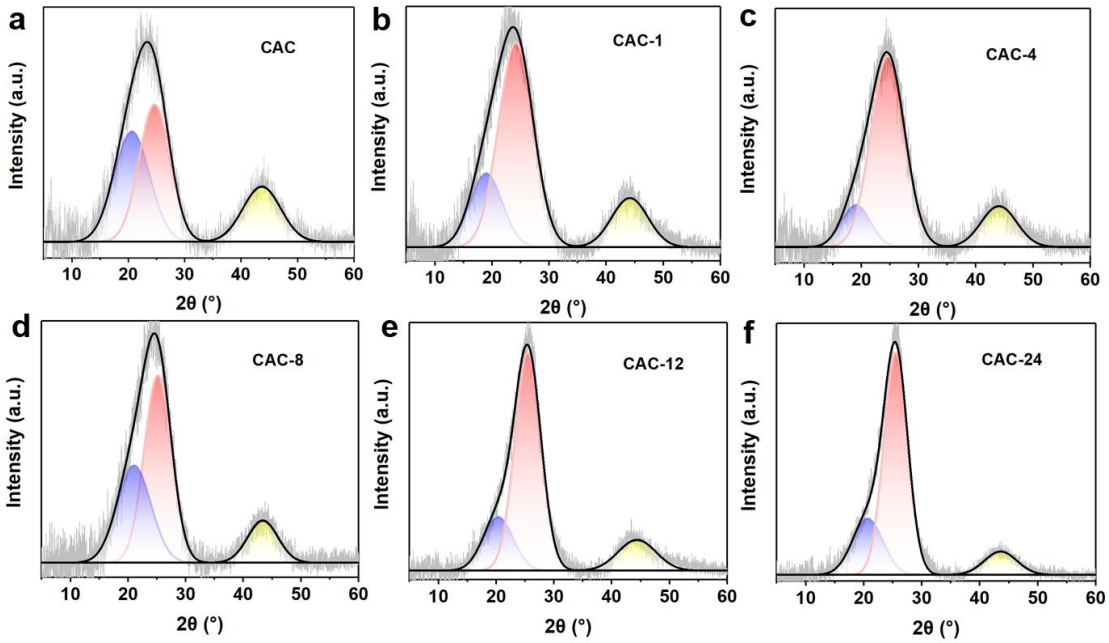

Figure S12 Deconvoluted XRD patterns of CAC and CAC-*x*.

Table S1 Structural parameters of microcrystals from XRD patterns for CAC and CAC-*x*.

	CAC	CAC-1	CAC-4	CAC-8	CAC-12	CAC-24
d_{002}	0.437	0.368	0.362	0.354	0.350	0.349
L_a	2.221	2.338	2.399	2.824	2.272	2.651
L_c	1.229	1.113	1.147	1.438	1.503	1.654

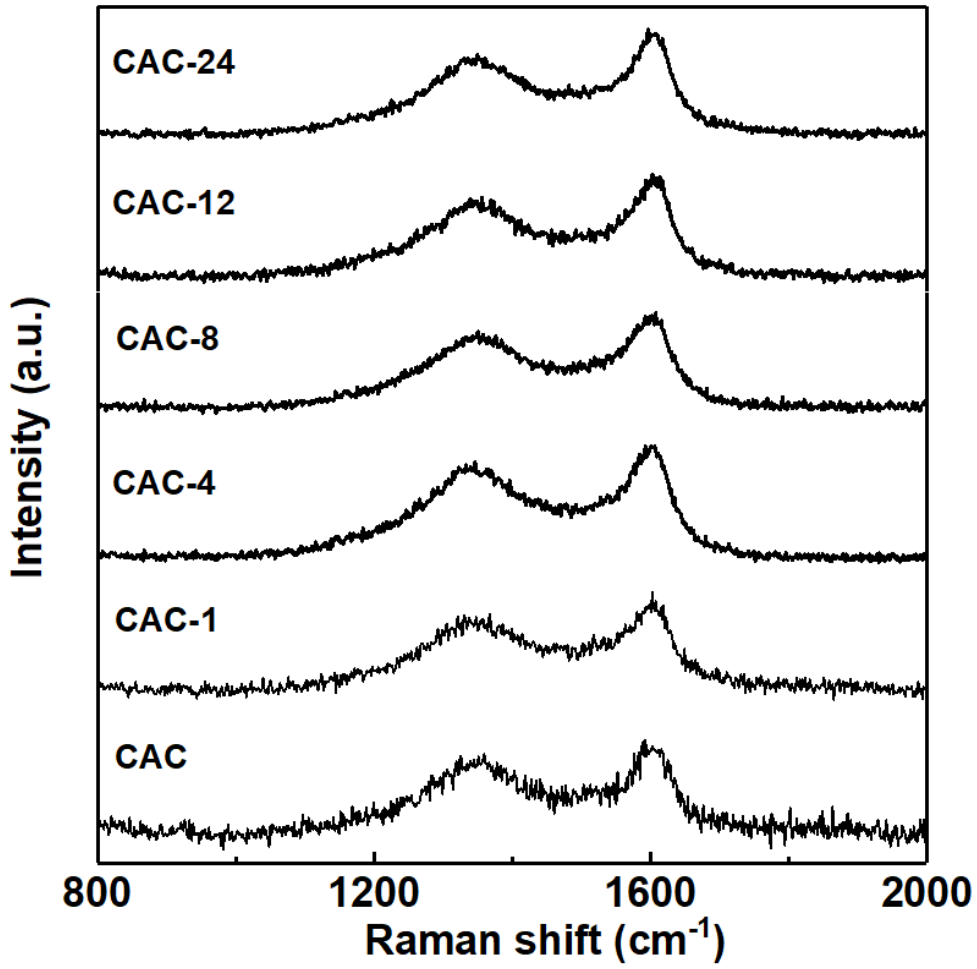

Figure S13 Raman patterns of CAC and CAC-*x*.

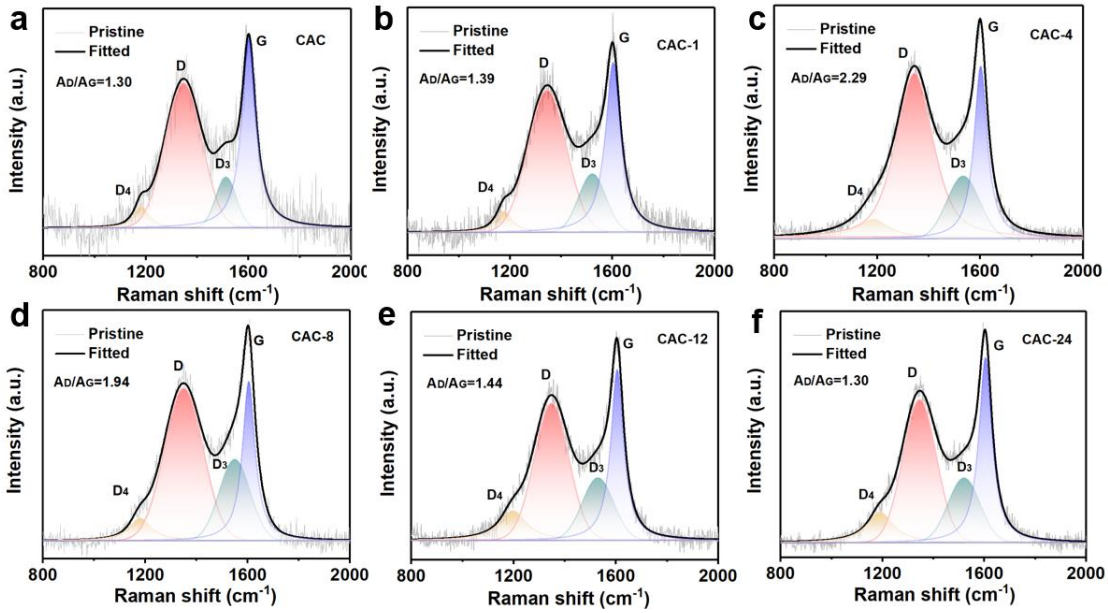

Figure S14 Deconvoluted Raman spectras of CAC and CAC-*x*.

Table S2 A_D/A_G from Raman patterns for CAC and CAC-*x*.

	CAC	CAC-1	CAC-4	CAC-8	CAC-12	CAC-24
A_D/A_G	1.30	1.39	2.29	1.94	1.44	1.30

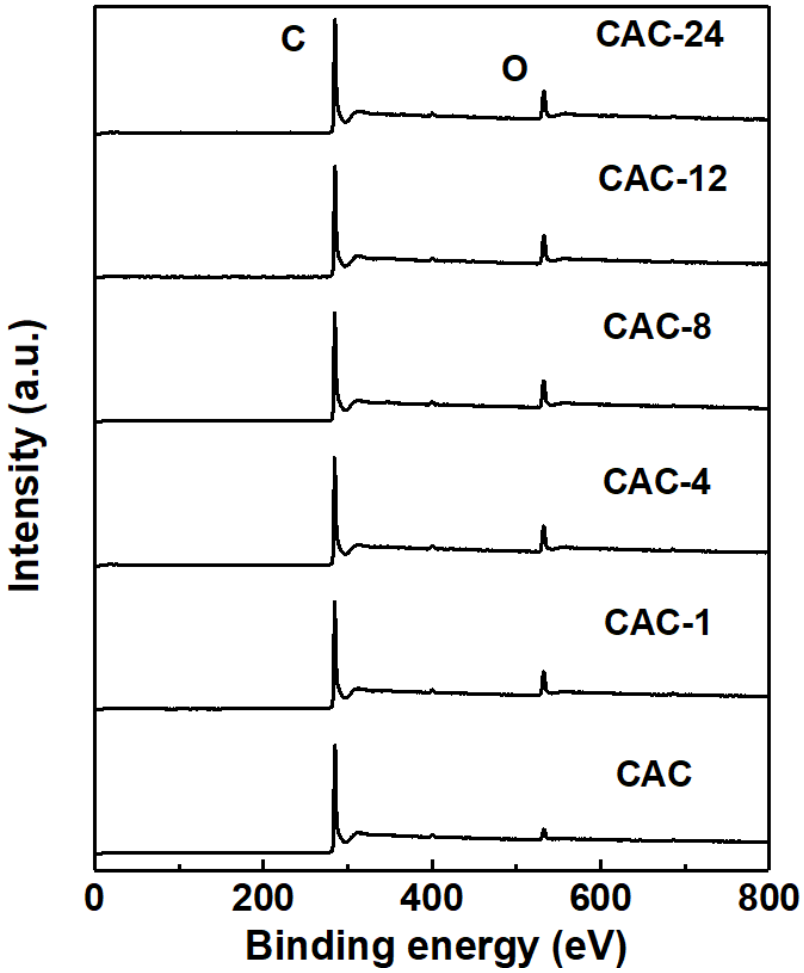

Figure S15 XPS patterns of CAC and CAC-*x*.

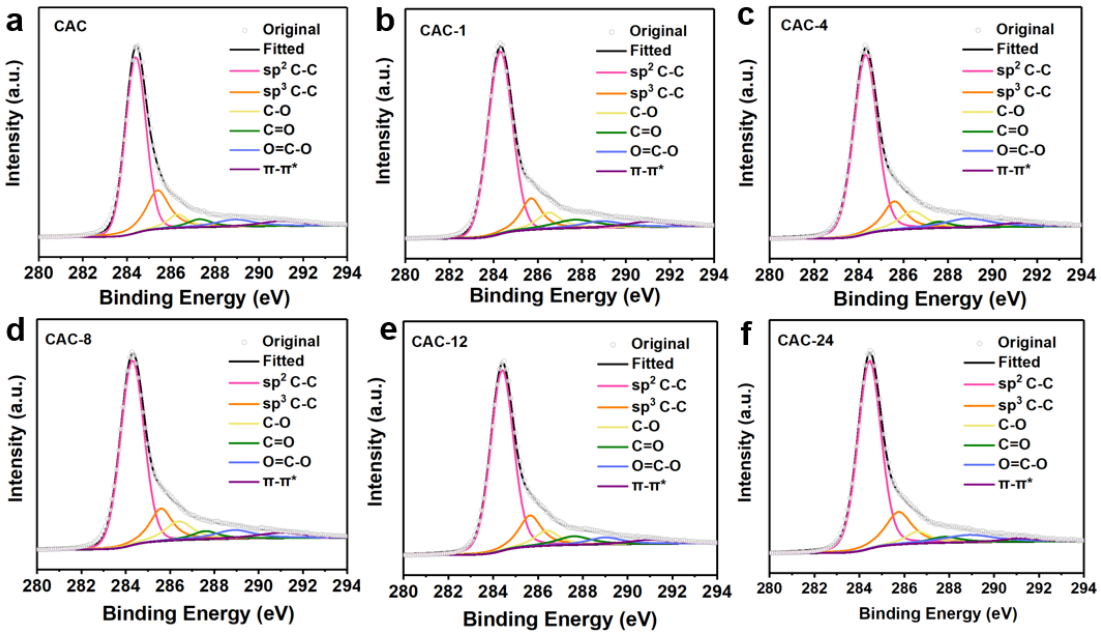

Figure S16 Deconvoluted C1s spectras of CAC and CAC-*x*.

Table S3 Contents of carbon and oxygen elements from XPS spectrum for CAC and CAC-*x*.

	CAC	CAC-1	CAC-4	CAC-8	CAC-12	CAC-24
*C*1s	94.25	88.77	87.79	87.67	87.62	87.84
*O*1s	5.75	11.23	12.21	12.33	12.38	12.16

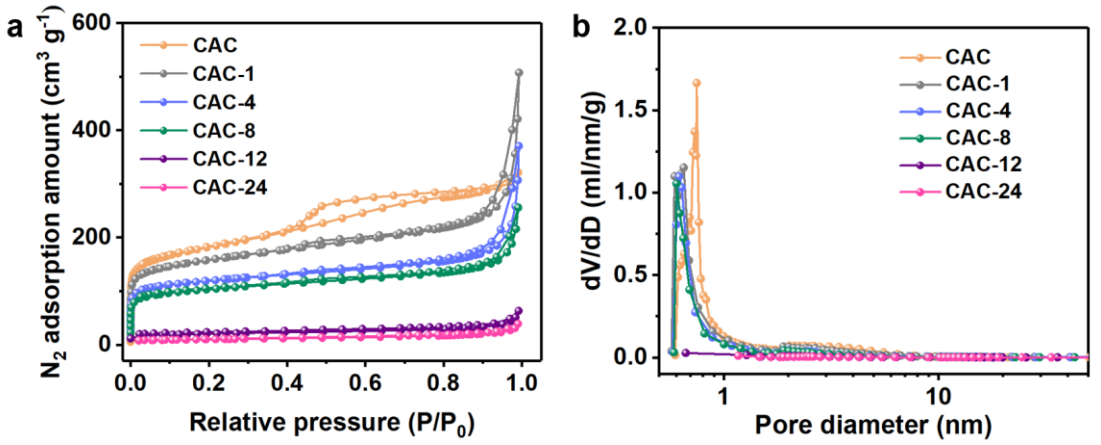

Figure S17 a N_2 adsorption–desorption isotherms and **b** pore size distribution of CAC and CAC-*x*.

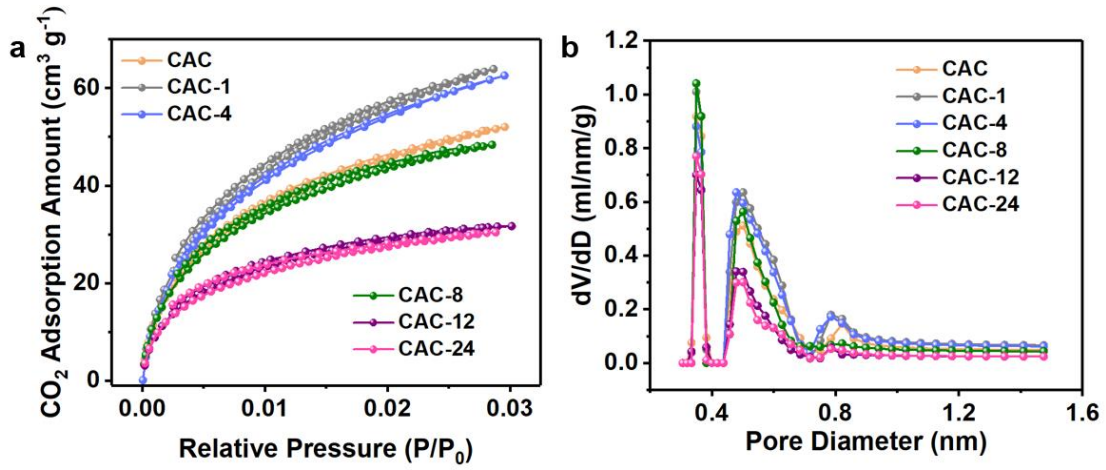

Figure S18 a CO_2 adsorption–desorption isotherms and **b** pore size distribution of CAC and CAC-*x*.

Table S4 Pore structure parameters of CAC and CAC-*x*.

	N2 adsorption						CO2 adsorption			
	S_{BET} m^2/g	S_{micro} m^2/g	V_{total} ml/g	V_{micro} ml/g	$V_{macro-meso}$ ml/g	D_a	S'_{BET} m^2/g	V'_{micro} ml/g	V'_{total}= V'_{micro}+$V_{macro-meso}$	V'_{micro}/ V'_{total}
CAC	605.18	265.85	0.50	0.13	0.37	3.28	537.30	0.151	0.521	0.290
CAC-1	510.65	396.12	0.69	0.22	0.47	5.38	670.92	0.193	0.663	0.291
CAC-4	381.24	270.81	0.49	0.14	0.35	5.11	647.24	0.187	0.537	0.348
CAC-8	335.02	228.87	0.39	0.12	0.27	4.62	502.45	0.138	0.408	0.338
CAC-12	66.84	42.97	0.09	0.02	0.07	5.64	326.48	0.086	0.156	0.551
CAC-24	33.48	13.45	0.06	0.01	0.05	7.19	314.39	0.083	0.133	0.624

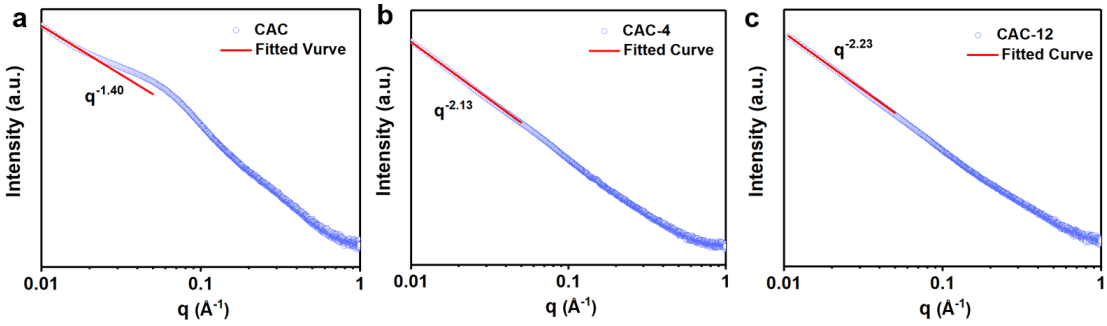

Figure S19 Fractal dimensions of CAC and CAC-*x*.

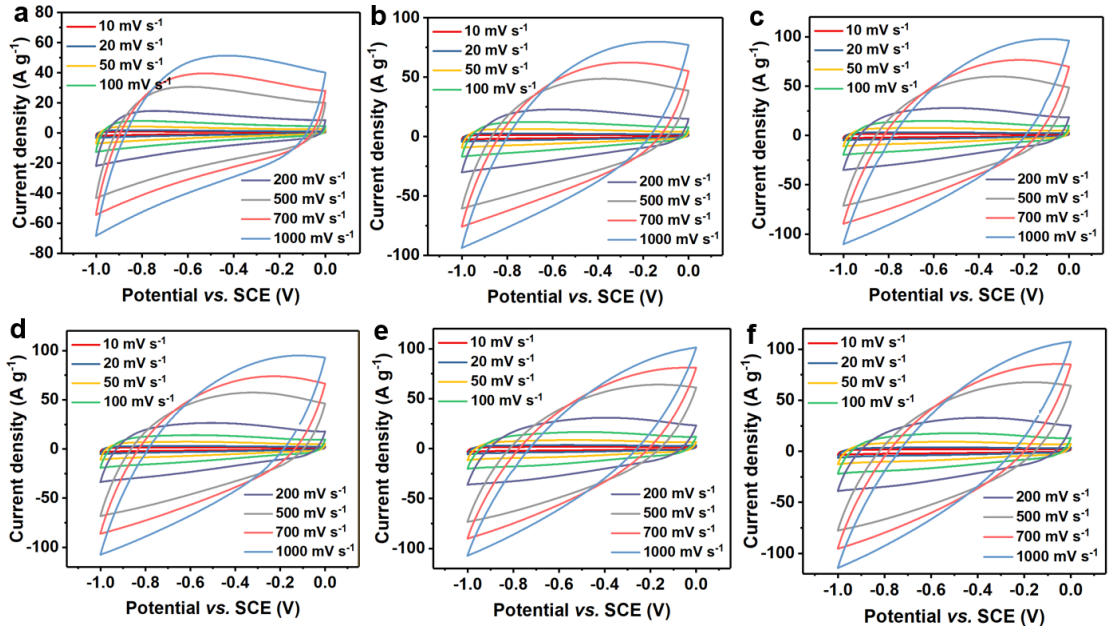

Figure S20 Cyclic voltammetry curves at various scan rates of **a** CAC, **b** CAC-1, **c** CAC-4, **d** CAC-8, **e** CAC-12 and **f** CAC-24 in a three-electrode system.

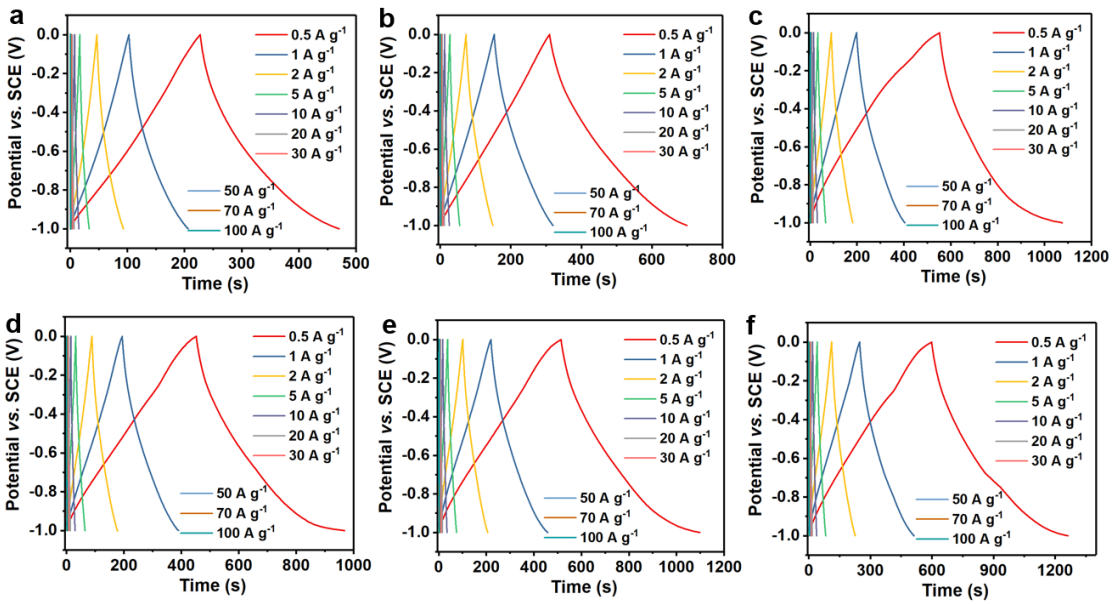

Figure S21 Galvanostatic charge/discharge (GC) at various current densities of **a** CAC, **b** CAC-1, **c** CAC-4, **d** CAC-8, **e** CAC-12 and **f** CAC-24 in a three-electrode system.

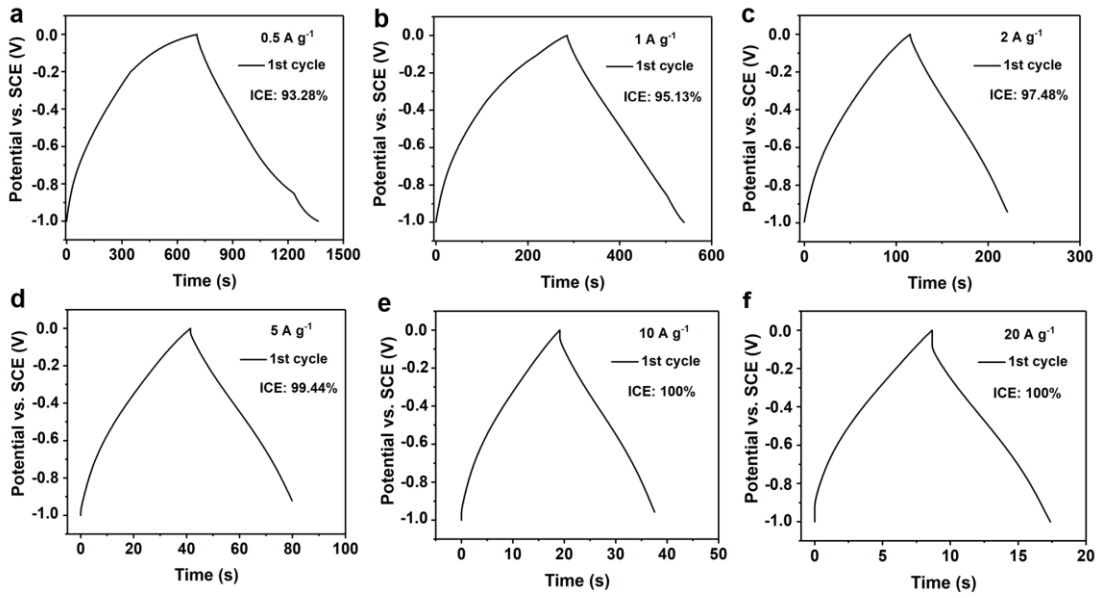

Figure S22 Initial two galvanostatic charge/discharge curves at various current densities of CAC-24 in a three-electrode system with Initial Coulombic Efficiency of **a** 93.28% at 0.5 A g^{-1}; **b** 95.13% at 1 A g^{-1}; **c** 97.48% at 2 A g^{-1}; **d** 99.44% at 5 A g^{-1}; **e** 100% at 10 A g^{-1}; **f** 100% at 20 A g^{-1}.

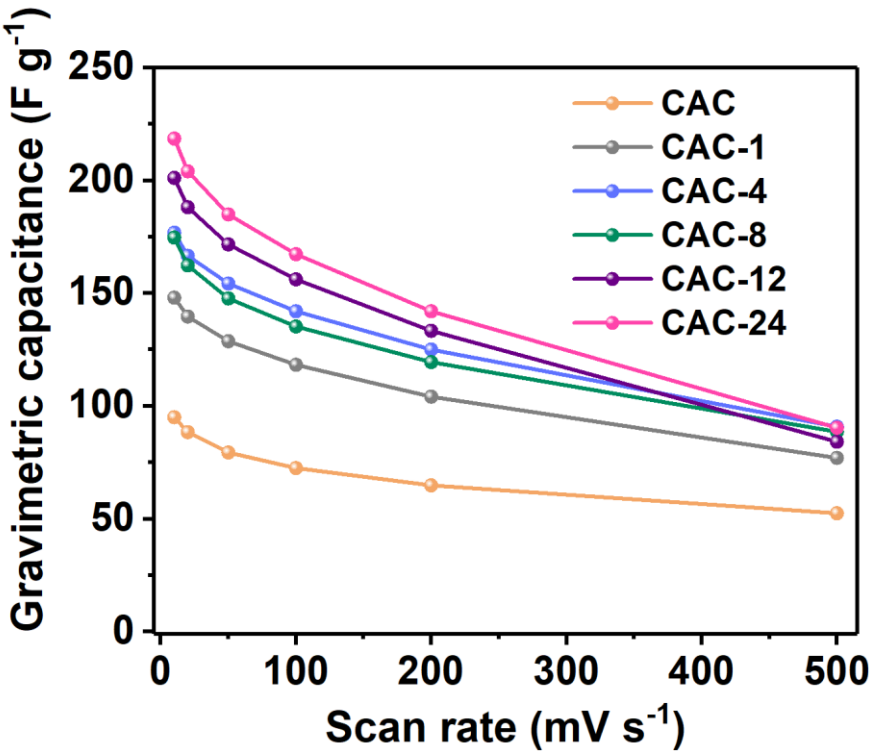

Figure S23 Gravimetric capacitances of CAC-*x* calculated from CV curves.

The specific gravimetric capacitances of CAC-x at various scan rates calculated based on CV curve integral were shown in **Figure S23**, showing that the specific gravimetric

capacitances gradually increase with the extension of ball milling time. Particularly, the specific gravimetric capacitance is calculated to be 219 F g^{-1} at 10 mV s^{-1}, which is nearly 2.3 times that of CAC (95 F g^{-1}) calculated based on CV curves.

Table S5 Material densities and electrode densities of CAC and CAC-*x*.

	CAC	CAC-1	CAC-4	CAC-8	CAC-12	CAC-24
ρ_M	1.000	0.840	1.010	1.124	1.695	1.786
ρ_E	0.637	0.749	1.006	1.062	1.158	1.158

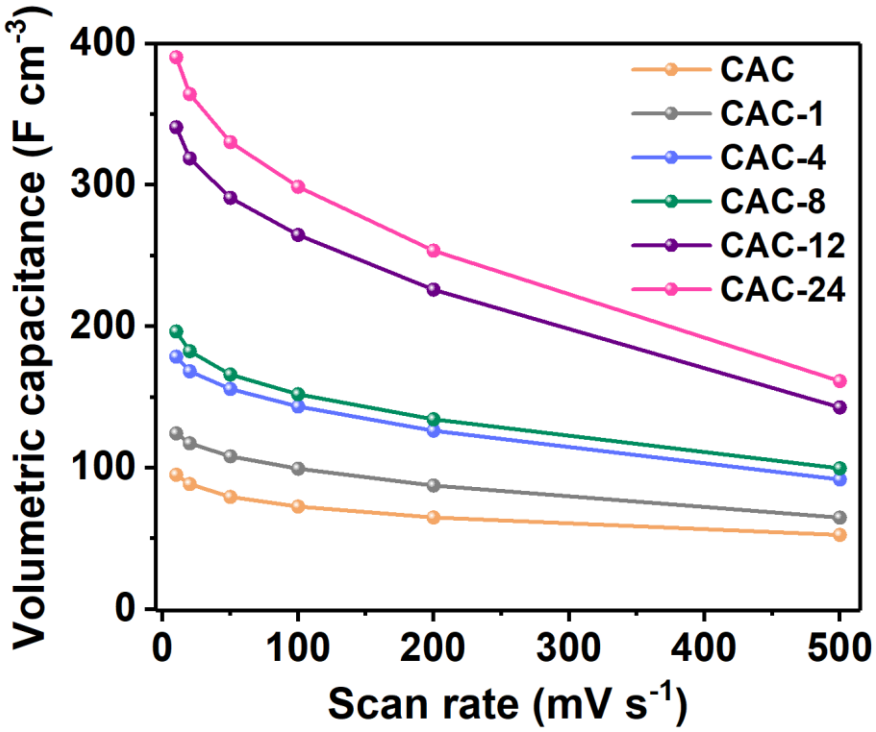

Figure S24 Volumetric capacitances of CAC-*x* calculated from CV curves based on material skeleton densities.

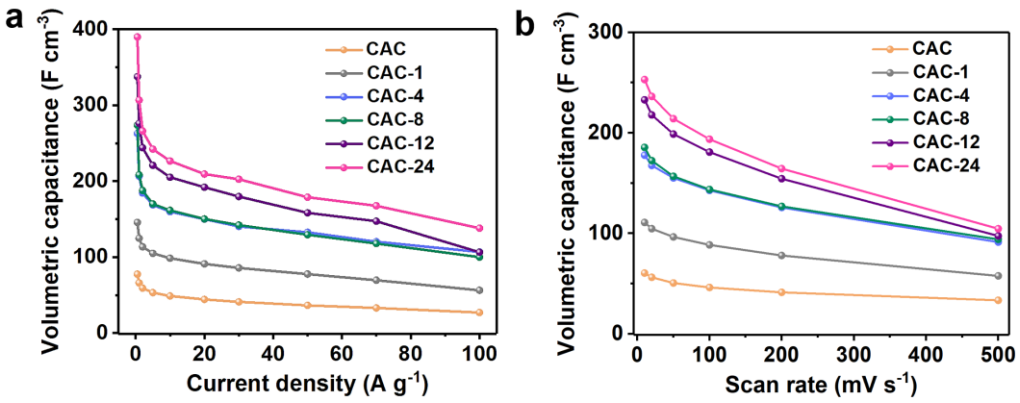

Figure S25 Volumetric capacitances of CAC-*x* based on electrode densities calculated from **a** GC curves and **b** CV curves.

Table S6 Comparison of pore parameters and capacitance properties in the literature.

Electrode material	Specific surface area (S_{BET})	Pore volume (V_{total})	Gravimetric specific capacitance (C_{wt})	Volumetric specific capacitance (C_v)	Reference
SGC-2	2927 $m^2 g^{-1}$	1.78 $cm^3 g^{-1}$	481 F g^{-1} @ 0.5 A g^{-1}	212 F cm^{-3} @ 0.5 A g^{-1}	[1]
NPCG	410.4 $m^2 g^{-1}$	0.56 $cm^3 g^{-1}$	305 F g^{-1} @ 2 mV s^{-1}	287 F cm^{-3} @ 2 mV s^{-1}	[2]
SBC-600	580 $m^2 g^{-1}$	0.41 $cm^3 g^{-1}$	425 F g^{-1} @ 0.5 A g^{-1}	468 F cm^{-3} @ 0.5 A g^{-1}	[3]
N-AC/Gr1	1412.9 $m^2 g^{-1}$	0.68 $cm^3 g^{-1}$	379 F g^{-1} @ 0.05 A g^{-1}	258 F cm^{-3} @ 0.05 A g^{-1}	[4]
MAC/Gr	915 $m^2 g^{-1}$	0.43 $cm^3 g^{-1}$	339 F g^{-1} @ 0.05 A g^{-1}	365 F cm^{-3} @ 0.05 A g^{-1}	[5]
GPC-600	2045m^2/g	0.99 $cm^3 g^{-1}$	353 F g^{-1} @ 1 A/g	237 F cm^{-3} @ 1 A/g	[6]
BNOC-BU-W	778.02 $m^2 g^{-1}$	0.34 $cm^3 g^{-1}$	238 F g^{-1} @ 0.5 A g^{-1}	309 F cm^{-3} @ 0.5 A g^{-1}	[7]

BPNOCN F-45	379.02 $m^2 g^{-1}$	0.34 $cm^3 g^{-1}$	332 F g^{-1} @ 1 A g^{-1}	395 F cm^{-3} @ 1 A g^{-1}	[8]
POGH-30	249 $m^2 g^{-1}$	0.56 $cm^3 g^{-1}$	257 F g^{-1} @ 0.5 A g^{-1}	241 F cm^{-3} @ 0.5 A g^{-1}	[9]
ACMF-F	800 $m^2 g^{-1}$	0.50 $cm^3 g^{-1}$	384 F g^{-1} @ 1.0 A g^{-1}	384 F cm^{-3} @ 1.0 A g^{-1}	[10]
CAC	33 $m^2 g^{-1}$	0.06 $cm^3 g^{-1}$	337 F g^{-1} @ 0.5 A g^{-1}	602 F cm^{-3} @ 0.5 A g^{-1}	This work

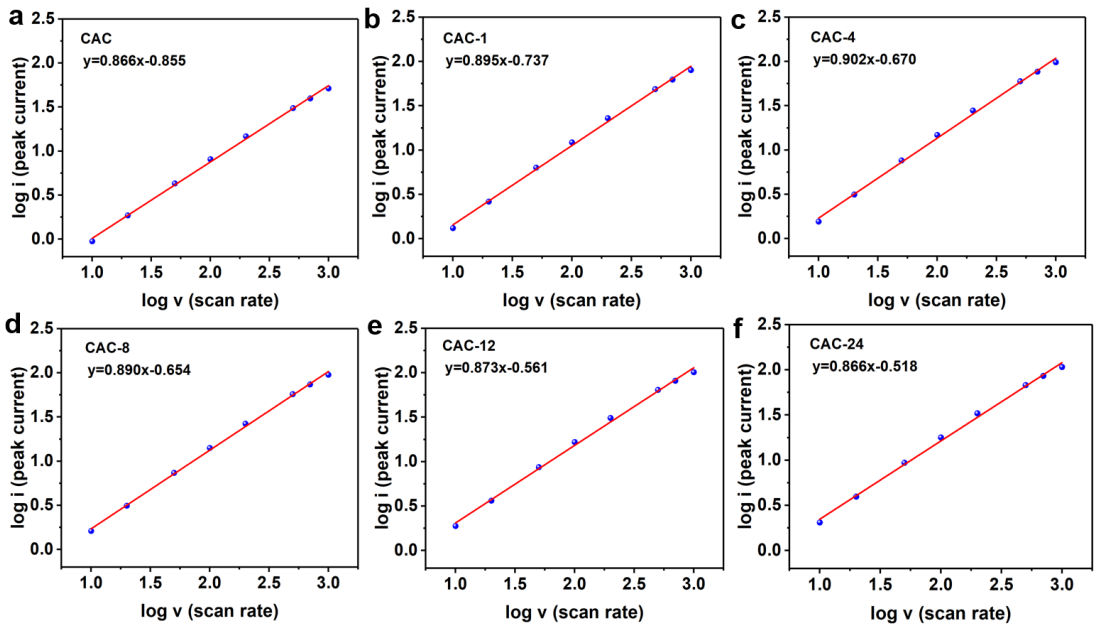

Figure S26 B values calculated from CV profiles of **a** CAC, **b** CAC-1, **c** CAC-4, **d** CAC-8, **e** CAC-12 and **f** CAC-24.

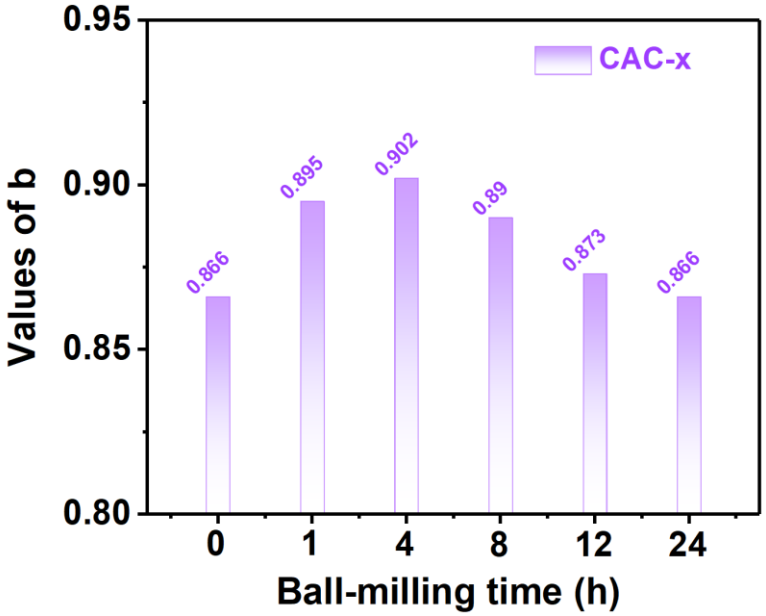

Figure S27 The corresponding b values of CAC and CAC-*x*.

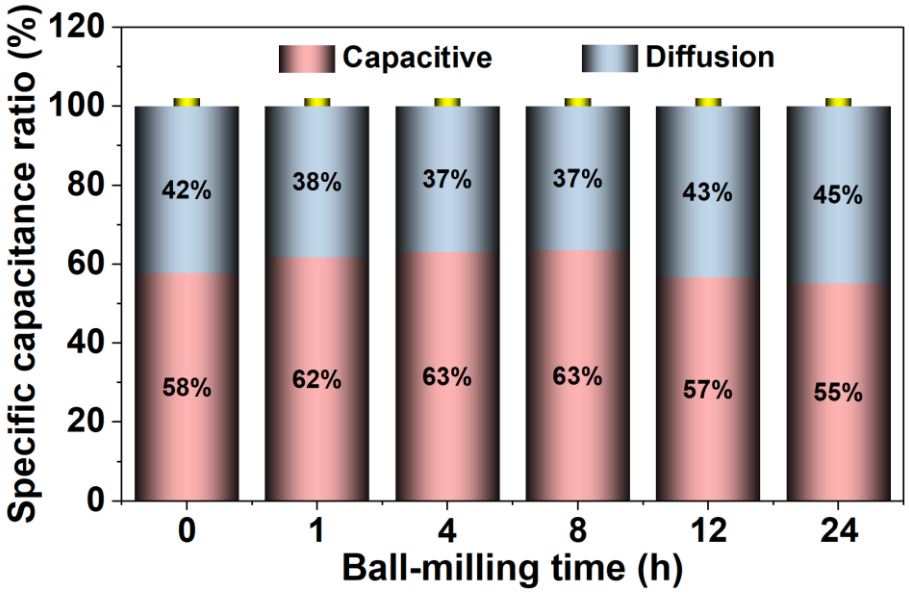

Figure S28 Ratios of capacitive-controlled contributions and diffusion-controlled contributions of CAC-*x* and CAC-*x* electrodes.

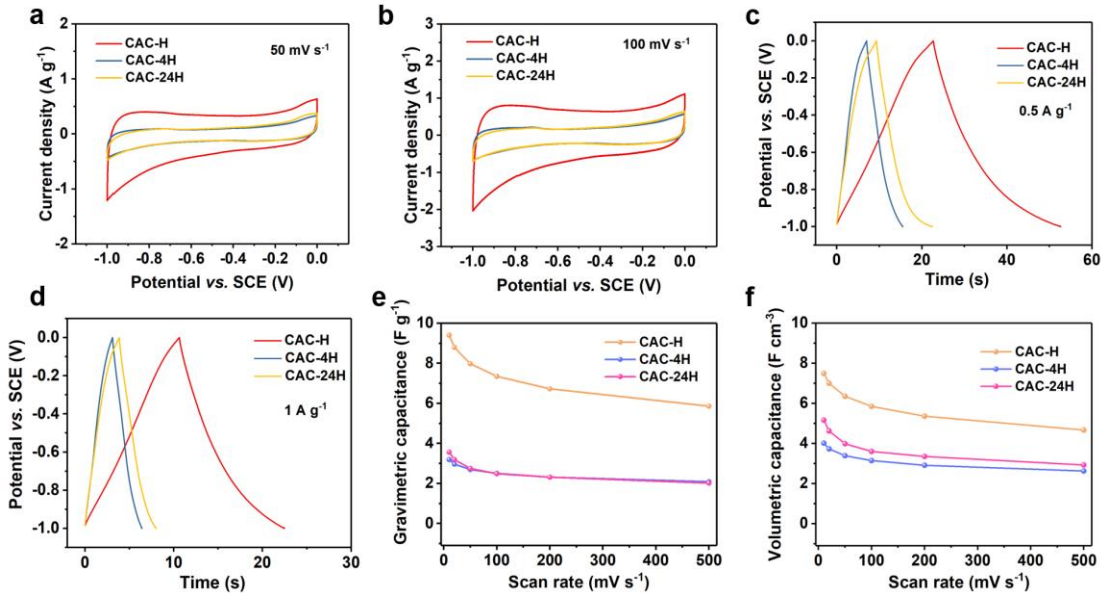

Figure S29 Electrochemical performances of CAC-H, CAC-4H and CAC-24H electrodes in a three-electrode system using 6M KOH as electrolyte. **a** CV curves at 50 mV s^{-1} and **b** at 100 mV s^{-1} of CAC-H, CAC-4H and CAC-24H. **c** GC curves at 0.5 A g^{-1} and **d** at 1 A g^{-1} of CAC-H, CAC-4H and CAC-24H. **e** Gravimetric capacitances of CAC-H, CAC-4H and CAC-24H calculated from CV curves. **f** Volumetric capacitances of CAC-H, CAC-4H and CAC-24H based on electrode densities.

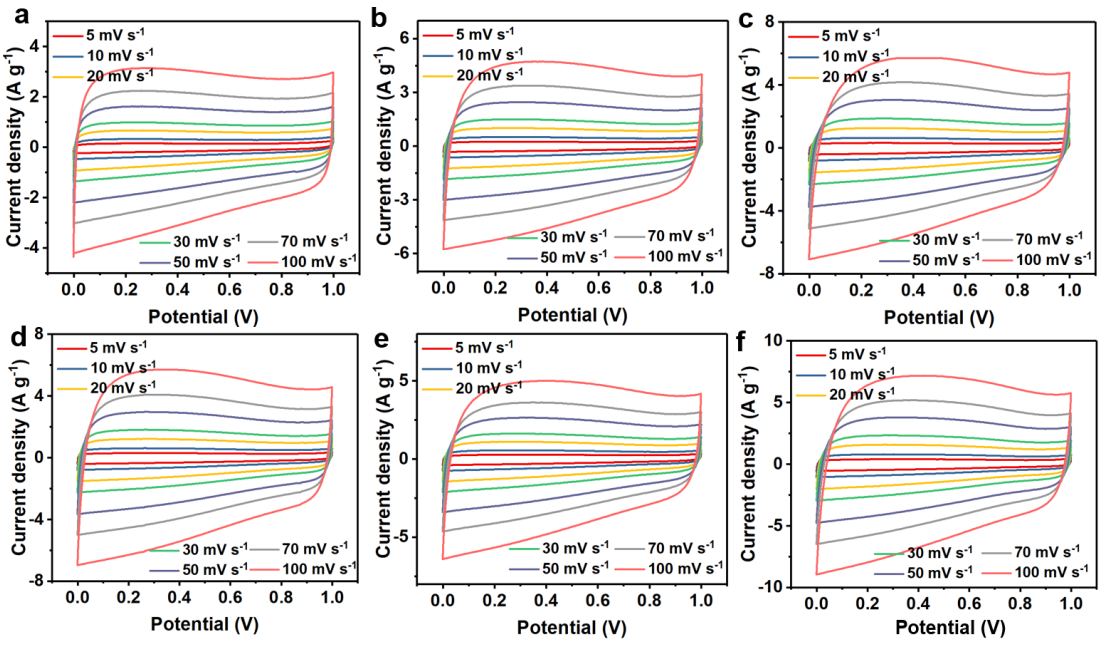

Figure S30 Cyclic voltammetry curves at various scan rates of **a** CAC, **b** CAC-1, **c** CAC-4, **d** CAC-8, **e** CAC-12 and **f** CAC-24 in aqueous symmetric supercapacitors.

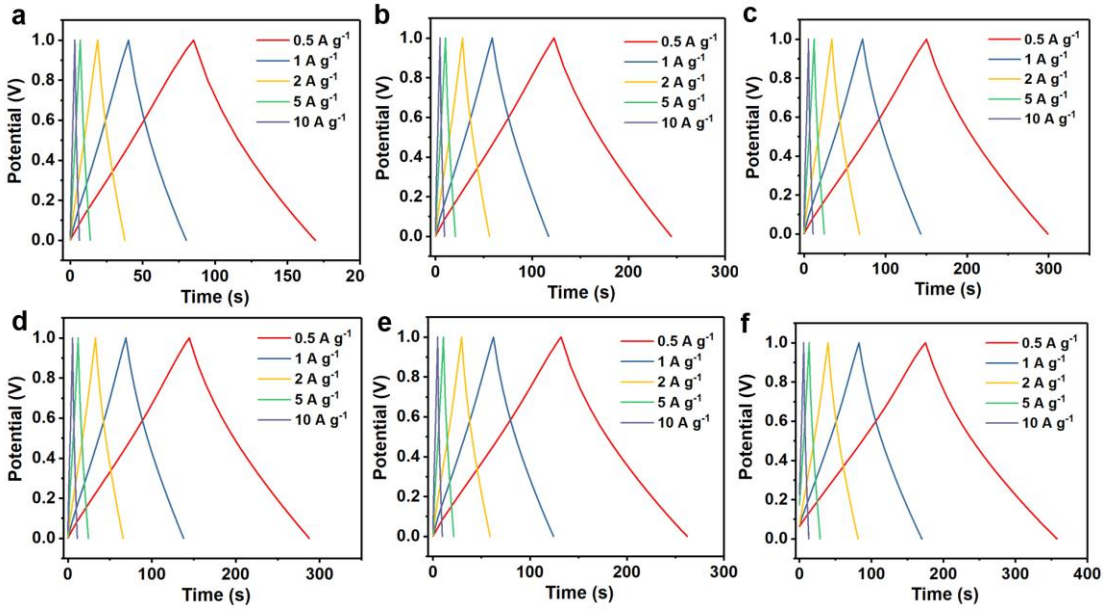

Figure S31 Galvanostatic charge/discharge (GC) at various current densities of **a** CAC, **b** CAC-1, **c** CAC-4, **d** CAC-8, **e** CAC-12 and **f** CAC-24 in aqueous symmetric supercapacitors.

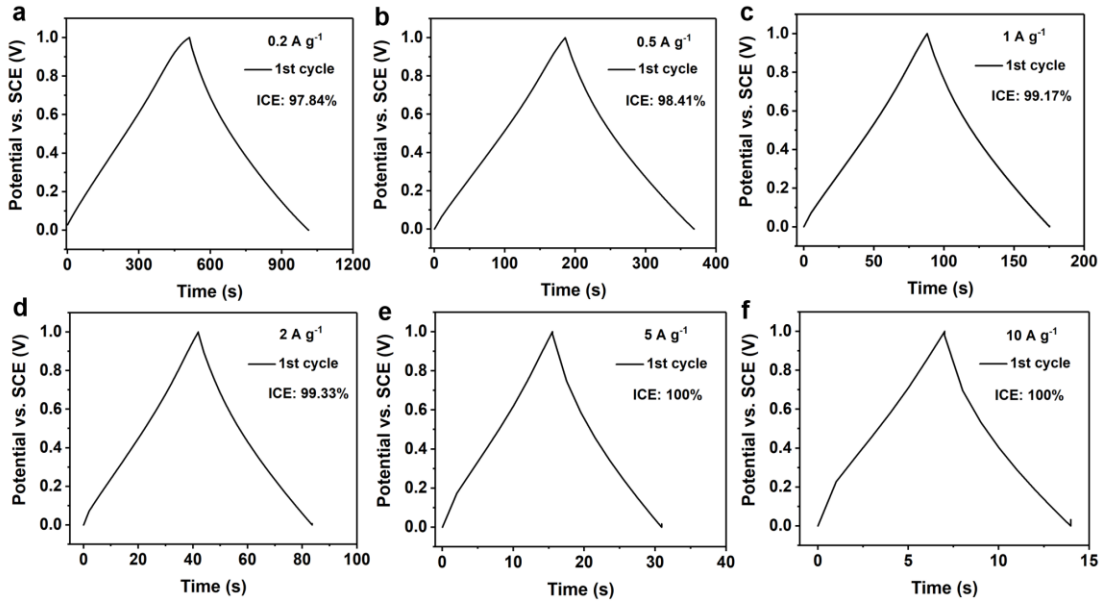

Figure S32 Initial two galvanostatic charge/discharge curves at various current densities of CAC-24 based symmetric supercapacitors with Initial Coulombic Efficiency of **a** 97.84% at 0.2 A g^{-1}; **b** 98.41% at 0.5 A g^{-1}; **c** 99.17% at 1 A g^{-1}; **d** 99.33% at 2 A g^{-1}; **e** 100% at 5 A g^{-1}; **f** 100% at 10 A g^{-1}.

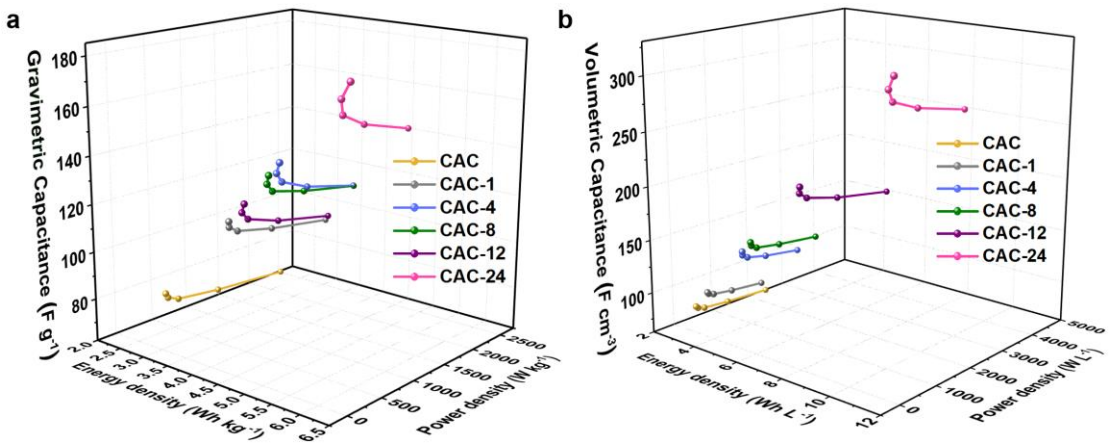

Figure S33. Relations of the capacitance, energy density, and power density in terms of **a** mass and **b** volume.

Based on the calculation method, relations of the capacitance, energy density, and power density in terms of mass and volume are shown in **Figure S33**. Due to its highest capacitance and density, the CAC-24-based symmetrical capacitor possesses the highest gravimetric energy density and volumetric energy density.

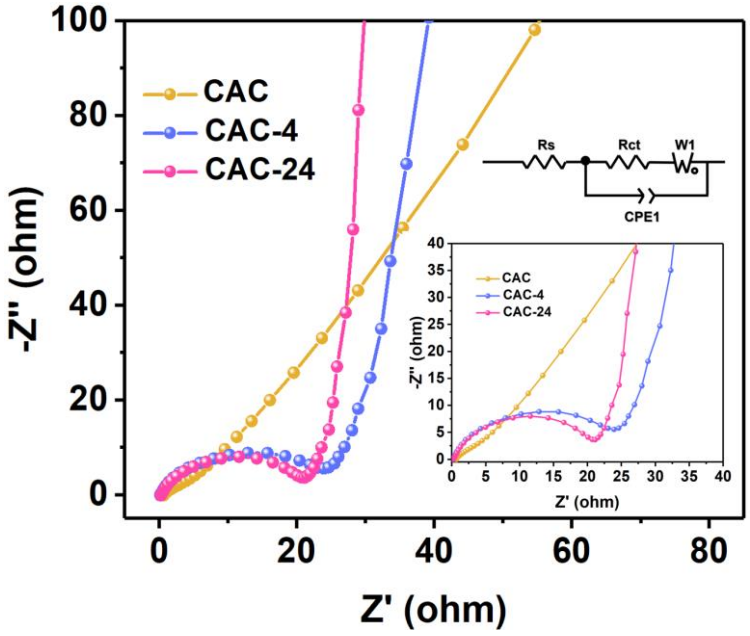

Figure S34 The comparison of Nyquist plots of CAC-*x* before CV and GC tests illustrated with corresponding equivalent circuits.

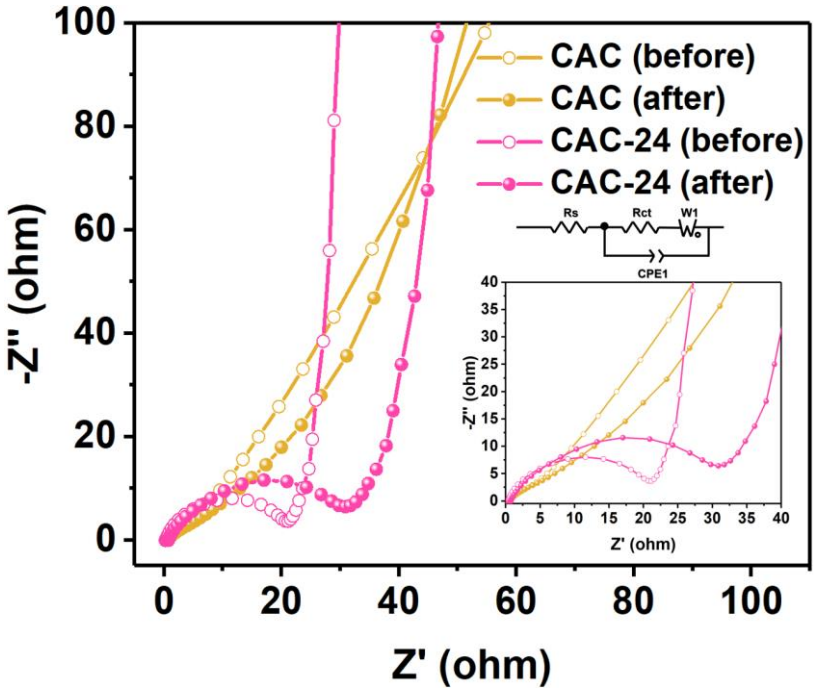

Figure S35 The comparison of Nyquist plots of CAC and CAC-24 before/after CV and GC tests illustrated with corresponding equivalent circuits.

Table S7 Comparison of the properties of CAC-24 based symmetric supercapacitors with other symmetric supercapacitors based on carbon materials in the literatures.

Electrode material	Electrolyte	Volumetric energy density	Cycling stability	Reference
POGH-30	6M KOH (0-1V)	8.3 Wh L^{-1} @116.9 W L^{-1}	100% after 10000 cycles @10 A g^{-1}	[9]
SGC-2	1 M Na_2SO_4 (0-1.8V)	11.32 Wh L^{-1} @45 W L^{-1}	--	[1]
SBC-600	6M KOH (0-1V)	13.2 Wh L^{-1} @350 W L^{-1}	--	[3]
N-AC/Gr1	6M KOH (0-1V)	11.1 Wh L^{-1} @10.6 W L^{-1}	93% after 10000 cycles @2 A g^{-1}	[4]
MAC/Gr	6M KOH (0-1V)	12.7 Wh L^{-1} @13.4 W L^{-1}	95% after 2000 cycles @5 A g^{-1}	[5]

BNOC-BU-W	6M KOH (0-1V)	11.5 Wh L^{-1} @622 W L^{-1}	92% after 3000 cycles @5 A g^{-1}	[7]
BPNOCNF-45	6M KOH (0-1V)	10 Wh L^{-1} @300 W L^{-1}	88% after 10000 cycles @5 A g^{-1}	[8]
CAC-24	6M KOH (0-1V)	11.32 Wh L^{-1} @223 W L^{-1}	96% after 10000 cycles @5 A g^{-1}; 85% after 30000 cycles @5 A g^{-1}	This work

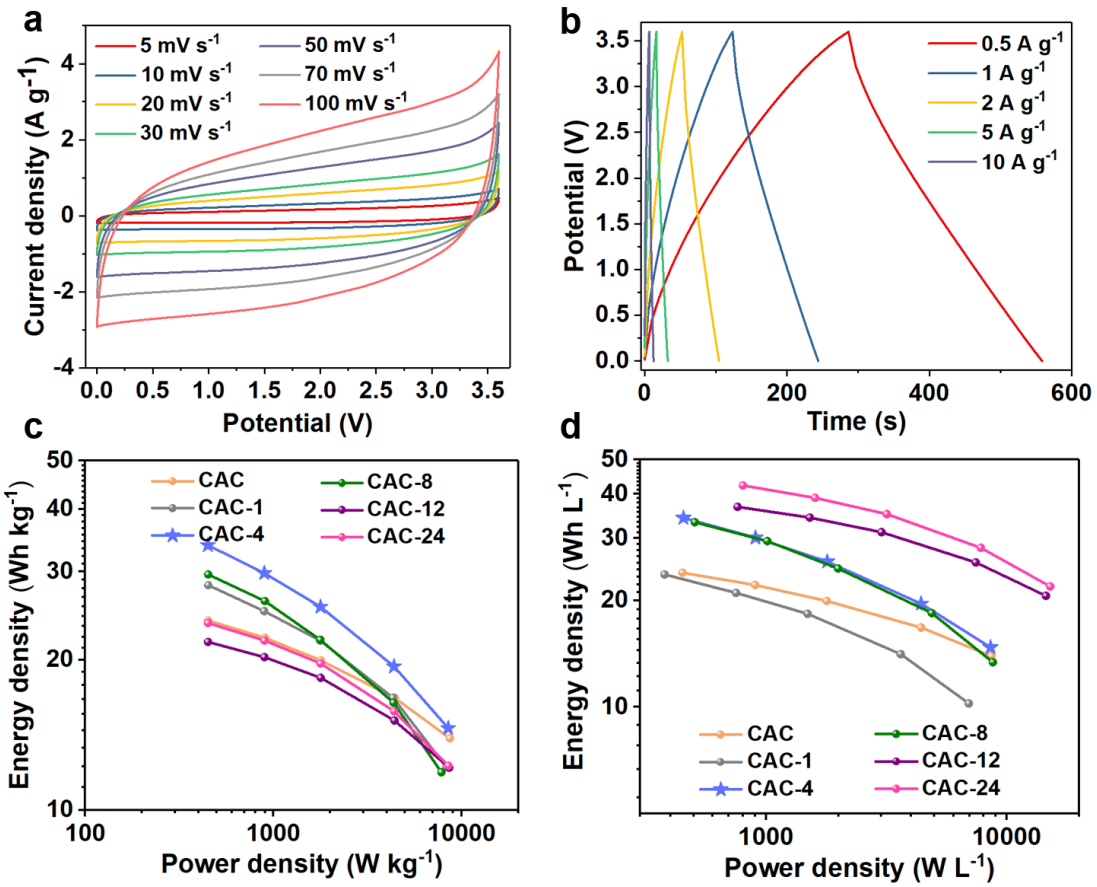

Figure S36 Electrochemical performances of symmetric supercapacitors using $EMIMBF_4$ ion liquid as electrolyte. a CV curves at various scan rates of CAC-4 symmetric supercapacitors in $EMIMBF_4$ ionic liquid electrolyte. **b** GC curves at various

current densities of CAC-4 symmetric supercapacitors. **c** Gravimetric energy densities of CAC-*x* symmetric supercapacitors. **d** Volumetric energy densities of CAC-*x* symmetric supercapacitors.

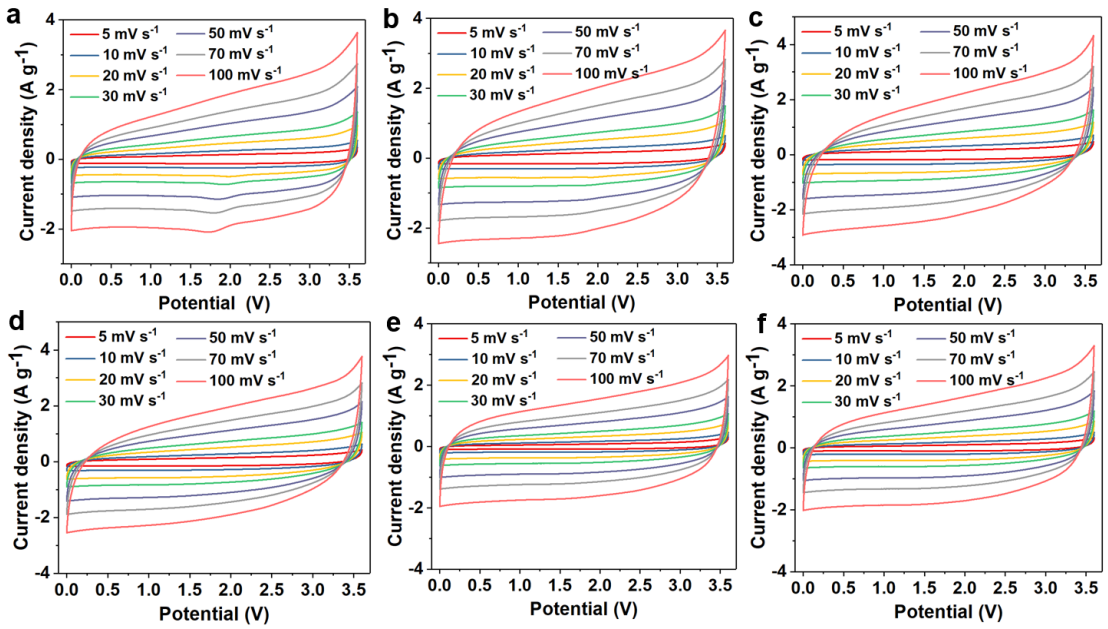

Figure S37 Cyclic voltammetry curves at various scan rates of **a** CAC, **b** CAC-1, **c** CAC-4, **d** CAC-8, **e** CAC-12 and **f** CAC-24 in ion liquid symmetric supercapacitors.

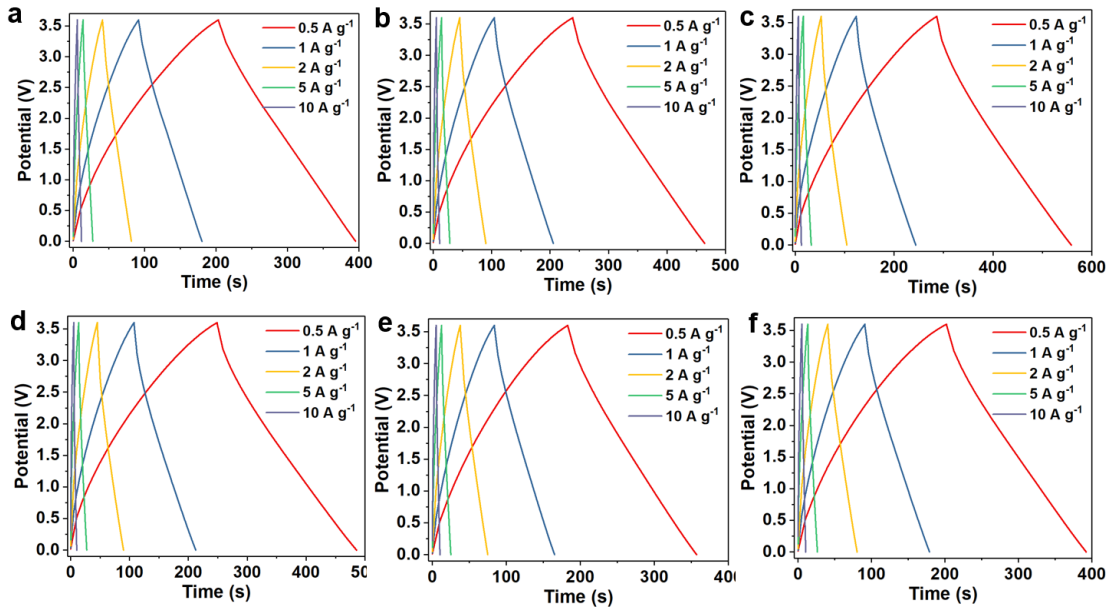

Figure S38 Galvanostatic charge/discharge (GC) at various current densities of **a** CAC, **b** CAC-1, **c** CAC-4, **d** CAC-8, **e** CAC-12 and **f** CAC-24 in ion liquid symmetric supercapacitors.

References

1. Yan J, Wang Q, Lin C, et al. Interconnected Frameworks with a Sandwiched Porous Carbon Layer/Graphene Hybrids for Supercapacitors with High Gravimetric and Volumetric Performances. *Advanced Energy Materials* 2014;4.

2. Wang Q, Yan J, Fan Z. Nitrogen-doped sandwich-like porous carbon nanosheets for high volumetric performance supercapacitors. *ELECTROCHIMICA ACTA* 2014;146:548-55.

3. Long C, Jiang L, Wu X et al. Facile synthesis of functionalized porous carbon with three-dimensional interconnected pore structure for high volumetric performance supercapacitors. *Carbon* 2015;93:412-20.

4. Xie Q, Bao R, Zheng A et al. Sustainable Low-Cost Green Electrodes with High Volumetric Capacitance for Aqueous Symmetric Supercapacitors with High Energy Density. *Acs Sustainable Chemistry & Engineering* 2016;4:1422-30.

5. Xie Q, Chen G, Bao R et al. Polystyrene foam derived nitrogen-enriched porous carbon/graphene composites with high volumetric capacitances for aqueous supercapacitors. *Microporous and Mesoporous Materials* 2017;239:130-7.

6. Mo R-J, Zhao Y, Zhao M-M et al. Graphene-like porous carbon from sheet cellulose as electrodes for supercapacitors. *Chemical Engineering Journal* 2018;346:104-12.

7. Wang C, Zhang X, Wang J et al. Boron/Nitrogen/Oxygen Co-Doped Carbon with High Volumetric Performance for Aqueous Symmetric Supercapacitors. *JOURNAL OF THE ELECTROCHEMICAL SOCIETY* 2018;165:A856-A66.

8. Ma Y, Zhang X, Liang Z et al. B/P/N/O co-doped hierarchical porous carbon nanofiber self-standing film with high volumetric and gravimetric capacitance performances for aqueous supercapacitors. *ELECTROCHIMICA ACTA* 2020;337.

9. Zhang Y, Fan S, Li S et al. 3D porous oxygen-enriched graphene hydrogels with well-balanced volumetric and gravimetric performance for symmetric supercapacitors. *Journal of Materials Science* 2020;55:12214-31.

10. Yao Y, Ge D, Yu Y et al. Filling macro/mesoporosity of commercial activated carbon enables superior volumetric supercapacitor performances. *Microporous and Mesoporous Materials* 2023;350.